# Supporting Information

## Agam et al. 10.1073/pnas.1103475108

### SI Methods

**Antisaccade Paradigm.** Before scanning, participants practiced the antisaccade paradigm in a mock MRI scanner and were encouraged to respond as quickly and accurately as possible. In addition to a base rate of pay, they received US $0.05 for each correct response, an incentive intended to enhance attention and motivation.

The antisaccade paradigm was programmed using MATLAB Psychtoolbox (MathWorks). It was composed of a pseudorandom sequence of three types of antisaccade trials that were balanced for right and left stimuli. Randomly interleaved with the saccadic trials were intervals of fixation lasting 2, 4, or 6 s, which provided a baseline and introduced "temporal jitter" to optimize the analysis of rapid presentation event-related fMRI data (1–3). The schedule of events was determined using a technique that optimizes the statistical efficiency of event-related designs (4). Each run of the task lasted 5 min and 16 s and generated an average of 64 antisaccade trials and 20 fixation epochs. Participants performed eight runs in EEG/MEG and six runs in fMRI. The order of EEG/MEG and fMRI sessions was counterbalanced across participants.

Each antisaccade trial lasted 4 s and began with an instructional cue at the center of the screen, either a blue or yellow "X." The cue indicated whether the trial was hard or easy, and the mapping of cue color to trial type was counterbalanced across participants. The cue was flanked horizontally by two small white squares with a width of 0.4° that marked the potential locations of stimulus appearance: 10° left and right of center. These squares remained visible for the duration of each run. At 300 ms, the instructional cue was replaced by a white fixation ring at the center of the screen, with a diameter of 1.3°. After 1,500 ms, the fixation ring disappeared for 200 ms. At 2,000 ms, the fixation ring reappeared at one of the two stimulus locations, right or left, with equal probability. This was the imperative stimulus to which the participant responded by making a saccade in the opposite direction. The ring remained in the peripheral location for 1,000 ms and then returned to the center, where participants were instructed to return their gaze for 1,000 ms before the start of the next trial. Fixation intervals were simply a continuation of the fixation display that constitutes the final second of the previous saccadic trial.

The three types of antisaccade trials were: hard (40%), easy (50%), and fake-hard (10%). Hard trials introduced a distraction during the gap, which consisted of a 3-dB luminance increase of the peripheral squares that mark the location of stimulus appearance. Fake-hard trials started with a cue indicating a hard trial but were otherwise identical to easy trials (i.e., there was no luminance change). They were included as a control condition to allow us to examine the effects of a hard vs. easy cue on fMRI activation unconfounded by the change in luminance that characterizes hard trials. Because this was not the goal of the present study, error and correct trials were combined across trial types for analysis. Posterror slowing was defined as the difference in response latency between correct trials immediately following an error and correct trials immediately preceding an error.

**Recording and Scoring of Eye Movement Data.** Eye movement data were scored offline using a partially automated MATLAB program. Saccades were identified as horizontal eye movements with velocities exceeding 47° per second. The onset of a saccade was defined as the point at which the velocity of the eye first exceeded 30° per second. For EEG/MEG analyses, only trials with initial saccade latencies over 110 ms were included in the analyses. The 110-ms cutoff excluded anticipatory saccades (5–7). Additionally, for EEG/MEG only, we excluded trials with eye blinks during the 100-ms baseline period before the saccade or in the 500 ms following the saccade.

**MRI Acquisition.** Twenty-eight participants were scanned with a 12-channel head coil, and 16 were scanned with a 32-channel head coil. Two high-resolution structural scans were acquired in the sagittal plane using a 3D rf-spoiled magnetization prepared rapid gradient echo (MPRAGE) sequence [12-channel: repetition time (TR)/echo time (TE)/flip angle = 2,530 ms/3.39 ms/7°, FOV = 256 mm, 176 in-plane sagittal slices sized 1.33 × 1 mm, 1.33-mm thickness; 32-channel: TR/TE/flip angle = 2,530 ms/1.61 + 1.78$n$ ms ($n$ = 0–3)/7°, integrated parallel acquisition techniques (iPAT) = 3, FOV = 256 mm, 176 in-plane sagittal slices sized 1 × 1 mm, 1-mm thickness]. Functional images were collected using a gradient echo T2*-weighted sequence (12-channel: TR/TE/flip angle = 2,000 ms/30 ms/90°, 32 contiguous horizontal slices parallel to the intercommissural plane, voxel size = 3.1 × 3.1 × 3.7 mm, interleaved; 32-channel: TR/TE/flip angle = 2,000 ms/28 ms/77°, iPAT = 3, 41 contiguous horizontal slices parallel to the intercommisural plane, voxel size = 3.1 × 3.1 × 3.1 mm, interleaved). The functional sequences included prospective acquisition correction (PACE) for head motion (8).

To construct the boundary-element model surface for each participant's MEG/EEG source estimation, we acquired a multiecho multiflip angle (5°) FLASH pulse sequence [610 Hz per pixel, TR = 20 ms, TE = 1.89 + 2$n$ ms ($n$ = 0–7), 128 in-plane sagittal slices sized 1 × 1.33 mm, 1.33-mm thickness].

Single-shot echo planar imaging DTI was acquired using a twice-refocused spin echo sequence with the following parameters: TR/TE = 7,980/84 ms, b = 700 s/mm$^2$, 10 T2 images acquired with b = 0, 60 diffusion directions, 128 × 128 matrix, 2 × 2 mm in-plane resolution, 64 axial oblique (anterior commissure-posterior commissure) slices, 2-mm (0-mm gap) slice thickness, scan duration = 9 min and 44 s.

**Surface-Based Analyses for fMRI and EEG/MEG Source Localization.** EEG/MEG source analyses and fMRI analyses were conducted on each participant's cortical surface, which was reconstructed using FreeSurfer (http://surfer.nmr.mgh.harvard.edu). MPRAGE scans were used to reconstruct inflated (2D) models of individual cortical surfaces using FreeSurfer segmentation, surface reconstruction, and inflation algorithms (9, 10). To register data across participants, functional and structural scans were spatially normalized using a surface-based spherical coordinate system employing a nonrigid alignment algorithm that explicitly aligns cortical folding patterns and is relatively robust to interindividual differences in the gyral and sulcal anatomy of cingulate cortex. Cortical activation was localized using automated surface-based parcellation software (11) that delineated the cingulate cortex and subdivided it into dorsal and rostral ACC and PCC regions (12). For group-level analysis, each participant's inflated cortical surface was registered to a template brain consisting of the averaged cortical surface of an independent sample of 40 adults from the Buckner laboratory at Washington University (St. Louis, MO) and implemented in Freesurfer.

**Preprocessing of EEG and MEG Data.** After excluding noisy EEG channels by visual inspection of the raw data, EEG data were rereferenced to the grand average. All MEG channels were

processed using the signal-space separation method (13). Each participant's continuous EEG and MEG data were low-pass-filtered at 40 Hz. Trials with eye blinks as defined by a difference between the maximum and minimum voltage of 150 μV or greater at the vertical EOG channel, were excluded from analysis. Response-locked data were baseline-corrected by subtracting the mean signal during the 100 ms preceding the response from the 500 ms of each trial that followed the response. Data for each of the two trial types (correct and error) were then averaged for each participant. Only trials meeting amplitude criteria were included (MEG: gradiometer peak-to-peak limit of 3,000 fT/cm and magnetometer peak-to-peak limit of 10 pT; EEG: peak-to-peak limit of 150 μV).

**Permutation Analysis for Multiple Comparisons Correction for Source Localization.** This analysis approximated the null distribution (i.e., no difference between correct and error trials) by randomly swapping the error and correct conditions for each participant (i.e., by multiplying each individual source estimate by either 1 or −1). This procedure was repeated 10,000 times. We then measured the area of the largest cluster of vertices with a significant nonzero current estimate ($P \leq 0.01$) in each permuted dataset, resulting in a distribution of cluster sizes. This null distribution was then used to determine the probability of the actually observed cluster size to occur by chance.

**Permutation Analysis for Comparison of PCC and dACC Time Courses.** To determine whether the 50-ms difference between the peaks of the current waveforms in the PCC and dACC was statistically significant, we used a permutation analysis, as in our prior study (14). This involved approximating the null distribution by calculating the difference in timing for 10,000 possible assignments of the data in the participants to the two regions and counting the proportion of these for which the absolute difference was greater than or equal to 50 ms. This enabled us to evaluate the null hypothesis of no difference in timing between the two regions.

**Analysis of fMRI Data.** In addition to online motion correction (PACE), functional scans were corrected retrospectively for motion using the analysis of functional neuroimages (AFNI) algorithm (15), intensity-normalized, and smoothed using a 3D 8-mm FWHM Gaussian kernel. Functional images were aligned to one of the two MPRAGE scans (selected based on image quality) for each participant. Finite impulse response estimates (2, 3) of the event-related hemodynamic responses were calculated for each trial type (e.g., error, correct) for each participant. This involved using a linear model to provide unbiased estimates of the average signal intensity at each time point for each trial type without making a priori assumptions about the shape of the hemodynamic response. Hemodynamic response estimates were computed at 12 time points with an interval of 2 s (corresponding to the TR), ranging from 4 s before the start of a trial to 18 s after the start. Temporal correlations in the noise were accounted for by prewhitening, using a global estimate of the residual error autocorrelation function truncated at 30 s (2). The data were registered across participants (*Methods*) and smoothed using a 2D 4.6-mm FWHM Gaussian kernel. To facilitate comparison with other studies, approximate Talairach coordinates were derived by mapping the surface-based coordinates of activation back to the original structural volume for each of the individuals whose brains were used to create the template brain, registering the volumes to the Montreal Neurological Institute (MNI305) atlas (16) and averaging the corresponding MNI305 coordinates. These coordinates were transformed to standard Talairach space using an algorithm developed by Matthew Brett (http://imaging.mrc-cbu.cam.ac.uk/imaging/MniTalairach).

We designated four ROIs comprising the dACC and PCC regions in each hemisphere. Based on prior anatomical and neuroimaging work (17), we focused on the dorsal division of the PCC, which is thought to play a role in cognitive and motor functions and is more likely to be involved in generating the ERN than the ventral PCC, which is part of the default network. ROIs were defined anatomically based on the work of Desikan et al (12). ROI boundaries were defined by lines drawn perpendicular to the intercommissural plane – at the mammillary bodies to distinguish between the dACC and PCC, at the anterior boundary of the genu of the corpus callosum to mark the anterior boundary of the dACC, and at the posterior boundary of the splenium of the corpus callosum to mark the end of the dorsal PCC. The superior and inferior boundaries of both ROIs were the dorsal extent of the cingulate sulcus and the corpus callosum, respectively.

We compared activation in the contrast of error vs. correct antisaccades at 6 s, which is the peak of error-related activation (18), using a random effects model. To correct for multiple comparisons, 10,000 Monte Carlo simulations of synthesized white Gaussian noise were run using the smoothing, resampling, and averaging parameters of the surface-based functional analysis to determine the likelihood that a cluster of a certain size would be found by chance for a given threshold ($P \leq 0.01$) on the cortical surface and to provide cluster-wise probability values.

**Functional Connectivity MRI Analysis.** The motion-corrected fMRI scans were registered to the Montreal Neurological Institute (MNI152) atlas (16) using the Functional MRI of the Brain Software Library (FSL, www.fmrib.ox.ac.uk/fsl). Additional preprocessing steps, described in previous reports (19–21), were (*i*) spatial smoothing using a Gaussian kernel of 6-mm FWHM; (*ii*) temporal filtering (0.009–0.08 Hz); and (*iii*) removal of spurious or nonspecific sources of variance by regression of the following variables: (*a*) the six movement parameters computed by rigid body translation and rotation in preprocessing, (*b*) the mean whole-brain signal, (*c*) the mean signal within the lateral ventricles, and (*d*) the mean signal within a deep white matter ROI. The first temporal derivatives of these regressors were included in the linear model to account for the time-shifted versions of spurious variance. Regression of each of these signals was computed simultaneously, and the residual time course (22) was retained for the correlation analysis. A functional connectivity map was created for each seed region by computing the Pearson correlation of the average signal across the voxels in the seed region and every other voxel in the brain. The correlation map of each individual was converted to a map of $z$ scores using a Fisher's $z$ transform. Determination of functional connectivity with the seeds was based on $t$ tests of the $z$ scores at each voxel and a false discovery rate threshold of $P \leq 0.01$.

**DTI Analysis.** Raw diffusion data were corrected for head motion and residual eddy current distortion by registering all images to the first acquired T2 (b = 0) image, using the FMRIB's linear image registration tool (FLIRT) (23) with a 12-df global affine transformation, available through the FSL software library. The diffusion tensor and FA volumes were reconstructed using the standard least-squares fit to the log diffusion signal (24). FA volumes were registered to the high-resolution structural (T1) volumes for each participant using the T2 (b = 0) volume as an intermediary. Interparticipant registration of individual FA maps to the Montreal Neurological Institute (MNI305) atlas was performed using each participant's T1 structural image, and the resulting transformation was applied to individual FA volumes. The Montreal Neurological Institute-normalized FA volumes were smoothed with a 3D Gaussian kernel with a 6-mm FWHM.

FA values were regressed on the average latency of self-correction on error trials based on the EOG data, with age included as a covariate. We restricted our analysis to voxels in the cingulum bundle, as defined by the Jülich histological atlas (25) and implemented in FSL. We controlled for multiple comparisons by

creating 10,000 random permutations of the data. For each permutation, corrective saccade latencies were randomly assigned to participants and FA values in each voxel within the cingulum bundle were regressed on the shuffled set of latency values. We then measured the volume of the largest cluster within the cingulum bundle (voxel-wise threshold: $P \leq 0.05$) for each permutation, resulting in a distribution of cluster volumes under the null hypothesis, from which we estimated the significance of our actual results.


1. Buckner RL, et al. (1998) Functional-anatomic correlates of object priming in humans revealed by rapid presentation event-related fMRI. *Neuron* 20:285–296.
2. Burock MA, Dale AM (2000) Estimation and detection of event-related fMRI signals with temporally correlated noise: a statistically efficient and unbiased approach. *Hum Brain Mapp* 11:249–260.
3. Miezin FM, et al. (2000) Characterizing the hemodynamic response: effects of presentation rate, sampling procedure, and the possibility of ordering brain activity based on relative timing. *Neuroimage* 11:735–759.
4. Dale AM (1999) Optimal experimental design for event-related fMRI. *Hum Brain Mapp* 8:109–140.
5. Fischer B, Breitmeyer B (1987) Mechanisms of visual attention revealed by saccadic eye movements. *Neuropsychologia* 25(1A):73–83.
6. Doricchi F, et al. (1997) Neural control of fast-regular saccades and antisaccades: an investigation using positron emission tomography. *Exp Brain Res* 116:50–62.
7. Straube A, Riedel M, Eggert T, Müller N (1999) Internally and externally guided voluntary saccades in unmedicated and medicated schizophrenic patients. Part I. Saccadic velocity. *Eur Arch Psychiatry Clin Neurosci* 249:1–6.
8. Thesen S, Heid O, Mueller E, Schad LR (2000) Prospective acquisition correction for head motion with image-based tracking for real-time fMRI. *Magn Reson Med* 44:457–465.
9. Dale AM, Fischl B, Sereno MI (1999) Cortical surface-based analysis. I. Segmentation and surface reconstruction. *Neuroimage* 9:179–194.
10. Fischl B, Sereno MI, Dale AM (1999) Cortical surface-based analysis. II: Inflation, flattening, and a surface-based coordinate system. *Neuroimage* 9:195–207.
11. Fischl B, et al. (2004) Automatically parcellating the human cerebral cortex. *Cereb Cortex* 14:11–22.
12. Desikan RS, et al. (2006) An automated labeling system for subdividing the human cerebral cortex on MRI scans into gyral based regions of interest. *Neuroimage* 31: 968–980.
13. Taulu S, Kajola M (2005) Presentation of electromagnetic multichannel data: The signal space separation method. *J Appl Phys* 97:1–10.
14. Moon SY, et al. (2007) Where left becomes right: A magnetoencephalographic study of sensorimotor transformation for antisaccades. *NeuroImage* 36:1313–1323.
15. Cox RW, Jesmanowicz A (1999) Real-time 3D image registration for functional MRI. *Magn Reson Med* 42:1014–1018.
16. Collins DL, Neelin P, Peters TM, Evans AC (1994) Automatic 3D intersubject registration of MR volumetric data in standardized Talairach space. *J Comput Assist Tomogr* 18:192–205.
17. Vogt BA, Vogt L, Laureys S (2006) Cytology and functionally correlated circuits of human posterior cingulate areas. *Neuroimage* 29:452–466.
18. Polli FE, et al. (2005) Rostral and dorsal anterior cingulate cortex make dissociable contributions during antisaccade error commission. *Proc Natl Acad Sci USA* 102: 15700–15705.
19. Van Dijk KRA, et al. (2010) Functional connectivity MRI: Theory, properties, and optimization. *J Neurophysiol* 103:297–321.
20. Fox MD, et al. (2005) The human brain is intrinsically organized into dynamic, anticorrelated functional networks. *Proc Natl Acad Sci USA* 102:9673–9678.
21. Vincent JL, et al. (2006) Coherent spontaneous activity identifies a hippocampal-parietal memory network. *J Neurophysiol* 96:3517–3531.
22. Ritter P, Villringer A (2006) Simultaneous EEG-fMRI. *Neurosci Biobehav Rev* 30: 823–838.
23. Jenkinson M, Smith S (2001) A global optimisation method for robust affine registration of brain images. *Med Image Anal* 5:143–156.
24. Basser PJ, Mattiello J, LeBihan D (1994) MR diffusion tensor spectroscopy and imaging. *Biophys J* 66:259–267.
25. Eickhoff SB, et al. (2005) A new SPM toolbox for combining probabilistic cyto-architectonic maps and functional imaging data. *NeuroImage* 25:1325–1335.


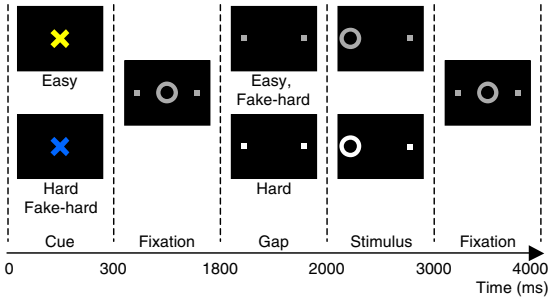


**Fig. S1.** Antisaccade paradigm. Schematic and time line of the three trial types: easy, hard, and fake-hard. Trials begin with an instructional cue (300 ms) of a color (blue or yellow) indicating either a hard or easy Trial, followed by fixation. At 1,800 ms, the central fixation ring disappears (200-ms gap), and at 2,000 ms, it reappears on either the right or left side as the imperative stimulus to which participants must respond. Hard trials are distinguished by an increase in luminance of both the peripheral squares that mark the potential locations of stimulus appearance during the gap and the imperative stimulus. Except for the hard cue, fake-hard trials are identical to easy trials. In the trials depicted, the correct response is a saccade away from the stimulus on the left side of the display. An error would involve a saccade toward the stimulus. After 1 s, the fixation ring returns to the center, where participants return their gaze to await the next trial.

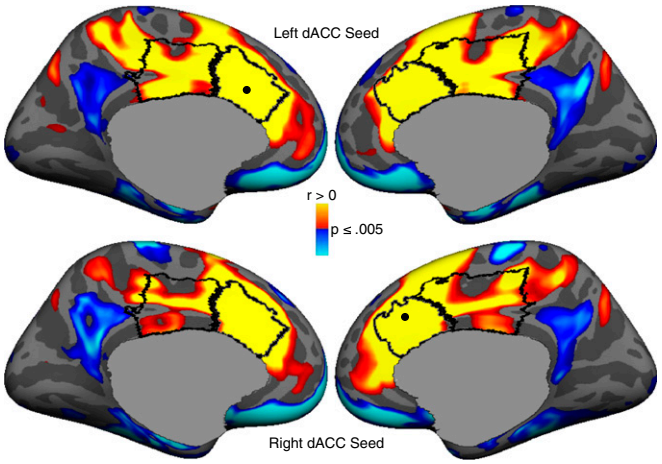


**Fig. S2.** Functional connectivity of the dACC during the resting state. Using the dACC seed regions centered on the fMRI maxima of error-related activation (black dots) from the present study, we analyzed resting state data from 45 participants (23 female, aged 22 ± 3 y; Buckner laboratory) in a public database (http://www.nitrc.org/projects/fcon_1000, details of scan parameters are provided on the Web site). The statistical maps are projected onto the cortical surface of the template brain. Activation in both the left dACC seed (*Upper*) and the right dACC seed (*Lower*) correlated with activation in the dorsal PCC. Warm and cool colors indicate positive and negative correlations, respectively.

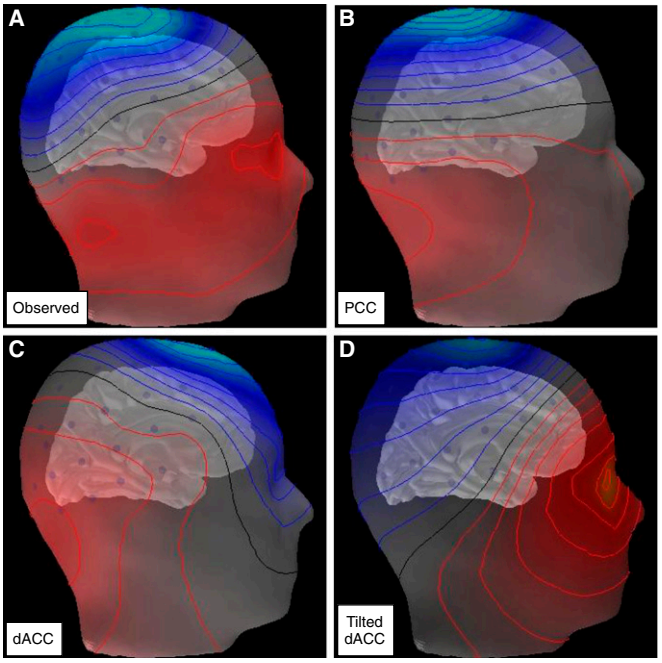


**Fig. S3.** Simulated scalp EEG patterns. (*A*) Distribution of the observed scalp potentials at the time of the peak ERN displayed on a head model of the template brain. (*B*) Simulation of the potential pattern generated by a simulated source at the observed maximal source in the PCC. (*C*) Potential pattern generated by a simulated source at the maximal error-related fMRI activation of the dACC. (*D*) Potential pattern generated by a simulated dACC dipole tilted 60° backward from the cortical surface normal orientation in the dACC.

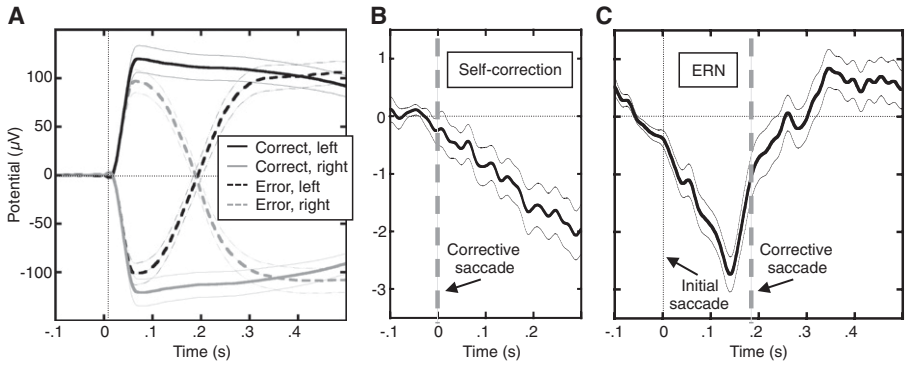


**Fig. S4.** Control analyses related to eye movements. (*A*) Response-locked horizontal EOG waveforms for correct and error trials to the left and right. (*B*) Averaged waveform at electrode Cz time-locked to corrective saccades (time 0) during error trials. Saccadic onset is marked by a vertical dashed gray line. (*C*) ERN (Fig. 2*B*) with a vertical dashed gray line indicating the mean time of the corrective saccade (179 ± 46 ms). In all plots, the thin lines on either side of the waveforms represent the SEM for each time sample.

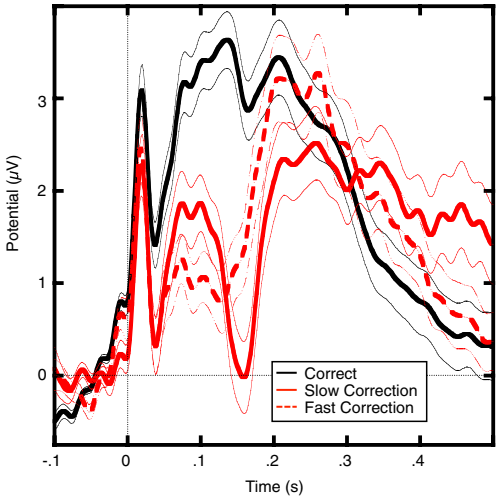


**Fig. S5.** Error waveforms for trials with fast vs. slow corrective saccades based on a median-split per subject. Grand average waveforms for correct (black) and error (red) trials, time-locked to the onset of the saccade. Note the more prominent late positivity (i.e., Pe) in the waveform for slow self-corrections. The thin lines represent the SEM waveform for each time sample.

**Table S1. Summary of ERN studies divided by response modality and measurement method (eye movements, EMG, button/key press)**

| Study | Task | Response | ERN peak scalp location | ERN peak latency, ms |
|---|---|---|---|---|
| Eye movement studies | | | | |
| Belopolsky and Kramer, 2006 (1) | Antisaccade + oculomotor capture | Saccade onset | Cz, CPz | 110 |
| Belopolsky et al., 2008 (2) | Oculomotor capture | Saccade onset | Pz | 80 |
| Endrass et al., 2005 (3) | Saccade countermanding | Saccade onset | Fz | 90 |
| Endrass et al., 2007 (4) | Antisaccade | Saccade onset | FCz | 100 |
| Nieuwenhuis et al., 2001 (5) | Antisaccade | Saccade onset | Cz | 80 |
| Wessel et al., 2011 (6) | Antisaccade | Saccade onset | — | 130 |
| EMG triggers | | | | |
| Burle et al., 2008 (7) | Flanker | EMG | — | 100 |
| Carbonnell and Falkenstein, 2006 (8) | Flanker | Force-sensitive devices | FCz | 83, 107 |
| Dhar et al., 2011 (9) | Go/no-go | EMG | FCz | 100 |
| Gehring et al., 1993 (10) | Flanker | EMG | — | 100 |
| Gehring and Fencsik, 2001 (11) | Manual Stroop | EMG onset | FCz | 165 |
| Holroyd et al., 1998 (12) | Flanker | Dynamometer squeeze | — | 100 |
| Kim et al., 2007 (13) | Go/no-go | EMG | — | 126 |
| Masaki et al., 2007 (14) | Simon | EMG | FCz | 140, 152 |
| Mathalon et al., 2003 (15) | Go/no-go | EMG | Cz | 125 |
| **9. Roger et al., 2010** (16) | Flanker | EMG | — | 109, 162 |
| Scheffers and Coles, 2000 (17) | Flanker | EMG | Cz | 100 |
| Van Boxtel et al., 2005 (18) | Stop-signal | EMG | Cz | 87 |
| Vidal et al., 2000 (19) | Go/no-go | EMG | FCz | 120 |
| Manual triggers | | | | |
| **1. Aarts and Pourtois, 2010** (20)* | Go/no-go | Key press | FCz | 50 |
| **2. Alain et al., 2002** (21)* | Stroop | Button | Cz | 40 |
| **3. Herrmann et al., 2004** (22) | Flanker | Button | — | 52 |
| **4. Hochman et al., 2009** (23) | Flanker | Joystick | — | 60, 70 |
| **5. Ladouceur et al., 2007** (24)* | Flanker | Button | Cz | 60 |
| **6. Mathewson et al., 2005** (25)* | Flanker, source memory | Key press | Cz, FCz | 60, 50 |
| **7. Munro et al., 2007** (26)* | Flanker | Key press | Cz | 75 |
| **8. O'Connell et al., 2007** (27)* | Modified Stroop | Button | FCz | 80 |
| **10. Santesso and Segalowitz, 2008** (28)* | Flanker, go/no-go | Button | FCz | 80 |
| **11. Segalowitz et al., 2010** (29)* | Flanker | Button | — | 70 |
| **12. van Schie et al., 2004** (30) | Flanker | Joystick | Cz | 80 |
| **13. van Veen and Carter, 2002** (31)* | Flanker | Button | Cz | 60 |
| **14. Vlamings et al., 2008** (32)* | Auditory decision | Button | FCz | n/a |
| **15. Vocat et al., 2008** (33)* | Go/no-go | Key press | FCz | 29 |

Numbered studies in bold font are those whose source coordinates are displayed in Fig. 1. The manual triggers category is restricted to studies that provided a source localization. A dash in the ERN peak scalp location column indicates that this information was not provided. More than one value in the ERN peak latency column indicates that more than one ERN was derived (e.g., for more than one task or type of error).

*Because the source localization method used in this study did not provide Talairach coordinates, they were estimated by a neuroanatomist (N.M.) based on anatomical landmarks.


1. Belopolsky AV, Kramer AF (2006) Error-processing of oculomotor capture. *Brain Res* 1081:171–178.
2. Belopolsky AV, Kramer AF, Theeuwes J (2008) The role of awareness in processing of oculomotor capture: Evidence from event-related potentials. *J Cogn Neurosci* 20:2285–2297.
3. Endrass T, Franke C, Kathmann N (2005) Error awareness in a saccade countermanding task. *J Psychophysiol* 19:275–280.
4. Endrass T, Reuter B, Kathmann N (2007) ERP correlates of conscious error recognition: Aware and unaware errors in an antisaccade task. *Eur J Neurosci* 26:1714–1720.
5. Nieuwenhuis S, Ridderinkhof KR, Blom J, Band GP, Kok A (2001) Error-related brain potentials are differentially related to awareness of response errors: Evidence from an antisaccade task. *Psychophysiology* 38:752–760.
6. Wessel JR, Danielmeier C, Ullsperger M (2011) Error awareness revisited: Accumulation of multimodal evidence from central and autonomic nervous systems. *J Cogn Neurosci* 23: 3021–3036.
7. Burle B, et al. (2008) Error negativity does not reflect conflict: a reappraisal of conflict monitoring and anterior cingulate cortex activity. *J Cogn Neurosci* 20:1637–1655.
8. Carbonnell L, Falkenstein M (2006) Does the error negativity reflect the degree of response conflict? *Brain Res* 1095:124–130.
9. Dhar M, Wiersema JR, Pourtois G (2011) Cascade of neural events leading from error commission to subsequent awareness revealed using EEG source imaging. *PLoS ONE* 6:e19578.
10. Gehring WJ, Goss B, Coles MG, Meyer DE, Donchin E (1993) A neural system for error detection and compensation. *Psychol Sci* 4:385–390.
11. Gehring WJ, Fencsik DE (2001) Functions of the medial frontal cortex in the processing of conflict and errors. *J Neurosci* 21:9430–9437.
12. Holroyd CB, Dien J, Coles MG (1998) Error-related scalp potentials elicited by hand and foot movements: Evidence for an output-independent error-processing system in humans. *Neurosci Lett* 242:65–68.
13. Kim EY, et al. (2007) Error-related negativity in a visual go/no-go task: children vs. adults. *Dev Neuropsychol* 31:181–191.
14. Masaki H, Falkenstein M, Stürmer B, Pinkpank T, Sommer W (2007) Does the error negativity reflect response conflict strength? Evidence from a Simon task. *Psychophysiology* 44: 579–585.
15. Mathalon DH, Whitfield SL, Ford JM (2003) Anatomy of an error: ERP and fMRI. *Biol Psychol* 64:119–141.
16. Roger C, et al. (2010) Rostral Cingulate Zone and correct response monitoring: ICA and source localization evidences for the unicity of correct- and error-negativities. *Neuroimage* 51: 391–403.
17. Scheffers MK, Coles MG (2000) Performance monitoring in a confusing world: Error-related brain activity, judgments of response accuracy, and types of errors. *J Exp Psychol Hum Percept Perform* 26:141–151.
18. van Boxtel GJM, van der Molen MW, Jennings JR (2005) Differential involvement of the anterior cingulate cortex in performance monitoring during a stop-signal task. *J Psychophysiol* 19:1–10.
19. Vidal F, Hasbroucq T, Grapperon J, Bonnet M (2000) Is the 'error negativity' specific to errors? *Biol Psychol* 51:109–128.

20. Aarts K, Pourtois G (2010) Anxiety not only increases, but also alters early error-monitoring functions. *Cogn Affect Behav Neurosci* 10:479–492.
21. Alain C, McNeely HE, He Y, Christensen BK, West R (2002) Neurophysiological evidence of error-monitoring deficits in patients with schizophrenia. *Cereb Cortex* 12:840–846.
22. Herrmann MJ, Römmler J, Ehlis AC, Heidrich A, Fallgatter AJ (2004) Source localization (LORETA) of the error-related-negativity (ERN/Ne) and positivity (Pe). *Brain Res Cogn Brain Res* 20:294–299.
23. Hochman EY, Eviatar Z, Breznitz Z, Nevat M, Shaul S (2009) Source localization of error negativity: Additional source for corrected errors. *Neuroreport* 20:1144–1148.
24. Ladouceur CD, Dahl RE, Carter CS (2007) Development of action monitoring through adolescence into adulthood: ERP and source localization. *Dev Sci* 10:874–891.
25. Mathewson KJ, Dywan J, Segalowitz SJ (2005) Brain bases of error-related ERPs as influenced by age and task. *Biol Psychol* 70:88–104.
26. Munro GE, et al. (2007) ERN varies with degree of psychopathy in an emotion discrimination task. *Biol Psychol* 76(1-2):31–42.
27. O'Connell RG, et al. (2007) The role of cingulate cortex in the detection of errors with and without awareness: A high-density electrical mapping study. *Eur J Neurosci* 25:2571–2579.
28. Santesso DL, Segalowitz SJ (2008) Developmental differences in error-related ERPs in middle- to late-adolescent males. *Dev Psychol* 44:205–217.
29. Segalowitz SJ, et al. (2010) Retest reliability of medial frontal negativities during performance monitoring. *Psychophysiology* 47:260–270.
30. van Schie HT, Mars RB, Coles MG, Bekkering H (2004) Modulation of activity in medial frontal and motor cortices during error observation. *Nat Neurosci* 7:549–554.
31. Van Veen V, Carter CS (2002) The timing of action-monitoring processes in the anterior cingulate cortex. *J Cogn Neurosci* 14:593–602.
32. Vlamings PH, et al. (2008) Reduced error monitoring in children with autism spectrum disorder: an ERP study. *Eur J Neurosci* 28:399–406.
33. Vocat R, Pourtois G, Vuilleumier P (2008) Unavoidable errors: a spatio-temporal analysis of time-course and neural sources of evoked potentials associated with error processing in a speeded task. *Neuropsychologia* 46:2545–2555.

**Table S2. ERN source localization based on combined EEG/MEG data**

| Cortical region | Cluster size, mm$^2$ | Direction of current | Approximate Talairach coordinates | | | Brodmann area | Maximum *P* value, -base-10 log | CWP |
|---|---|---|---|---|---|---|---|---|
| | | | x | y | z | | | |
| Left posterior cingulate sulcus | 778 | Out | −6 | −19 | 38 | 31 | 8.44 | 0.02 |
| Right posterior cingulate sulcus | 807 | Out | 10 | −13 | 36 | 24 | 7.04 | 0.02 |
| Left posterior cingulate gyrus | 971 | In | −7 | −29 | 29 | 23 | 6.07 | 0.01 |

Maxima and locations of clusters where dipole sources were significantly different from zero. Cluster-wise probabilities (CWPs) are based on correction for the entire cortical surface. *P* values are provided for the most significant dipole source in each cluster.

**Table S3. fMRI contrast of error vs. correct trials at 6 s**

| Cortical ROI | Cluster size, mm$^2$ | Direction of effect | Approximate Talairach coordinates | | | Brodmann area | Maximum *P* value, -base-10 log | CWP |
|---|---|---|---|---|---|---|---|---|
| | | | x | y | z | | | |
| Error-related activation | | | | | | | | |
| Left calcarine sulcus | 4,466 | E > C | −12 | −70 | 14 | 18 | 6.95 | 0.0001 |
| Right calcarine sulcus | 5,625 | E > C | 18 | −70 | 14 | 18 | 6.48 | 0.0001 |
| Right dACC | 2,844 | E > C | 13 | 23 | 30 | 32 | 4.97 | 0.0001 |
| Left circular insular sulcus | 708 | E > C | −29 | 30 | 1 | 13 | 4.82 | 0.0001 |
| Right inferior parietal lobule | 707 | C > E | 65 | −21 | 5 | 41 | 4.41 | 0.004 |
| Right circular insular sulcus | 1,541 | E > C | 34 | 30 | −2 | 13 | 4.29 | 0.0001 |
| Right precentral gyrus | 537 | C > E | 64 | −9 | 16 | 43 | 3.69 | 0.02 |
| Left dACC | 1,220 | E > C | −7 | 20 | 25 | 32 | 3.55 | 0.0001 |
| Regression of error-related activation on ERN amplitude | | | | | | | | |
| Right superior frontal gyrus | 1,213 | $r > 0$ | 7 | 39 | 43 | 8 | 6.25 | 0.0001 |
| Right posterior cingulate sulcus | 1,456 | $r > 0$ | 7 | −45 | 47 | 31 | 5.58 | 0.0001 |
| Left inferior parietal lobule | 772 | $r > 0$ | −54 | −48 | 28 | 40 | 5.89 | 0.002 |
| Right occipital pole | 1,468 | $r > 0$ | 12 | −80 | −5 | 18 | 4.73 | 0.0001 |
| Left circular insular sulcus | 1,378 | $r > 0$ | −46 | 15 | 7 | 13 | 4.41 | 0.0001 |
| Left posterior cingulate sulcus | 802 | $r > 0$ | −8 | −39 | 43 | 31 | 4.40 | 0.001 |
| Left cuneus gyrus | 1,395 | $r > 0$ | −7 | −77 | 31 | 18 | 4.07 | 0.0001 |
| Right circular insular sulcus | 1,678 | $r > 0$ | 41 | 29 | −6 | 13 | 4.05 | 0.0001 |
| Regression of error-related activation on error rate | | | | | | | | |
| Right circular insular sulcus | 591 | $r < 0$ | 33 | 16 | 1 | 13 | 3.69 | 0.01 |
| Left circular insular sulcus | 929 | $r < 0$ | −27 | 22 | −11 | 13 | 3.28 | 0.0002 |

Maxima and locations of significant clusters of error-related activation and of correlation with ERN amplitude and error rate. Cluster-wise probabilities (CWPs) are based on correction for the entire cortical surface. *P* values are provided for the most significant vertex in each cluster.

**Table S4. Functional connectivity of the dACC seed regions**

| Cortical ROI | Cluster size, $mm^2$ | Direction of correlation | Approximate Talairach coordinates | | | Brodmann area | Maximum *P* value, -base-10 log |
|---|---|---|---|---|---|---|---|
| | | | x | y | z | | |
| **Left dACC seed** | | | | | | | |
| Left dACC | 4,806 | $r > 0$ | −8 | 21 | 26 | 32 | 14.64 |
| Left PCC | | | −4 | −19 | 37 | 31 | 9.37 |
| Left superior frontal gyrus | | | −9 | 14 | 49 | 9 | 7.76 |
| Right dACC | 3,723 | $r > 0$ | 6 | 24 | 23 | 24 | 12.27 |
| Right PCC | | | 5 | −17 | 37 | 31 | 8.30 |
| Right middle frontal sulcus | 1,417 | $r > 0$ | 27 | 35 | 23 | 8 | 10.39 |
| Right intraparietal sulcus | 2,756 | $r < 0$ | 32 | −61 | 38 | 39 | 9.14 |
| Left insula | 3,034 | $r > 0$ | −38 | 30 | 0 | 13 | 8.51 |
| Left middle frontal sulcus | 1,681 | $r > 0$ | −23 | 38 | 22 | 9 | 8.31 |
| Right insula | 2,825 | $r > 0$ | 30 | 28 | 0 | 13 | 7.67 |
| Left angular gyrus | 1,280 | $r < 0$ | −31 | −66 | 42 | 19 | 6.27 |
| Right inferior temporal sulcus | 2,304 | $r < 0$ | 56 | −44 | −8 | 21 | 5.24 |
| **Right dACC seed** | | | | | | | |
| Left dACC | 3,531 | $r > 0$ | −7 | 17 | 27 | 24 | 10.51 |
| Left PCC | | | −5 | −14 | 37 | 31 | 6.31 |
| Left angular gyrus | 1,160 | $r < 0$ | −39 | −60 | 43 | 39 | 4.89 |
| Right dACC | 4,910 | $r > 0$ | 13 | 22 | 32 | 32 | 14.52 |
| Right superior frontal gyrus | | | 15 | 11 | 54 | 6 | 8.54 |
| Right PCC | | | 14 | −10 | 40 | 31 | 7.52 |
| Right middle frontal sulcus | 3,318 | $r > 0$ | 27 | 39 | 26 | 9 | 8.70 |
| Right insula | 1,594 | $r > 0$ | 42 | 14 | 6 | 13 | 6.54 |

Maxima and locations of clusters on the cortical surface. Only clusters larger than 1,000 $mm^2$ are listed. Local maxima (indented) are listed only if they were more than 20 mm from the global maximum and fell in a different Brodmann's area.